

https://dspace.org/

Rational construction of Ncontaining carbon sheets atomically doped NiPCoP nanohybrid electrocatalysts for enhanced green hydrogen and oxygen production

A Ipadeola; Mostafa Sliem; Patrick Mwonga; Kenneth Ozoemena; Aboubakr M Abdullah

https://hdl.handle.net/10539/42528
WOS

Downloaded from a DSpace repository. https://dspace.org/

Electrochimica Acta 508 (2024) 145236



Contents lists available at ScienceDirect

Electrochimica Acta

journal homepage: www.journals.elsevier.com/electrochimica-acta



Rational construction of N-containing carbon sheets atomically doped NiP-CoP nanohybrid electrocatalysts for enhanced green hydrogen and oxygen production

Adewale K. Ipadeola [a,*], Mostafa H. Sliem [a], Patrick Mwonga [b], Kenneth I. Ozoemena [b,*], Aboubakr M. Abdullah [a,*]

[a] Center for Advanced Materials, Qatar University, Doha 2713, Qatar
[b] Molecular Science Institute, School of Chemistry, University of the Witwatersrand, Private Bag 3, PO Wits, Johannesburg, 2050, South Africa

ARTICLE INFO

Keywords:
N-containing carbon composites
Hydrogen evolution reaction
Oxygen evolution reaction
Tafel slope
Exchange current density
H_2/O_2 production rate

ABSTRACT

The pursuit of sustainable energy production has directed rigorous research in the field of electrocatalysis, particularly for water electrolysis (i.e., hydrogen evolution (HER) and oxygen evolution reactions (OER)). This study discloses the rational synthesis of N-containing carbon sheets atomically doped NiP-CoP nanohybrid (NiP-CoP/NCS) via precipitation/calcination. The fabrication method tailored the physicochemical merits for collective contribution to improved green hydrogen and oxygen production, elucidated by surface/bulk characterization and theoretical calculations. Thus, the NiP-CoP/NCS had improved HER activity at lower overpotential (η_{10} = 197.7/274.6 mV), higher exchange current density (j_o = 0.71/0.67 mA/cm^2), turnover frequency (TOF = 2.63/1.47 s^{-1}), H_2 production rate (3601.63/2519.12 μmol/g/h) and superior stability after 24 h in acid/alkaline media, than NiP/NCS and CoP/NCS. Moreover, NiP-CoP/NCS delivered impressive OER activity at reduced η_{10} (309.1 mV), and Tafel slope (b_a = 58.9 ± 3.0 mV/dec), but higher TOF (3.67 s^{-1}) and O_2 production rate (3643.96 μmol/g/h) relative to NiP/NCS and CoP/NCS, besides higher stability for 24 h. These were further proved by theoretical calculations. This work indicates a deeper understanding of the fabrication methods of making efficient electrocatalysts for green and sustainable energy conversion.

1. Introduction

The exorbitant demands for energy consumption with attention to reducing carbon footprint have spurred a tremendous interest in renewable energy conversion and storage [1-3]. Water electrolysis is amongst the effective and environmentally benign approaches for generating renewable energy sources, including green hydrogen (H_2) and oxygen (O_2) production, achieved via hydrogen evolution (HER) and oxygen evolution reactions (OER), respectively [4-6]. Unlike other methods (i.e., natural gas, coal gasification, and steam reforming) with energy intensiveness and greenhouse emission [7-9], the HER enables the production of high-purity H_2 with no climate and environment impacts [10-12], and has a plethora of applications in proton exchange membrane fuel cells (PEMFCs), power stations, chemical/semiconductor industries, and space exploration. Whereas O_2 produced is applicable in metal-air batteries and glass industry [13-16]. Nevertheless, the HER and OER are driven by noble-metal based electrocatalysts (i.e., Pt, Pd, RuO_2), whose scarcity and costly nature limit their commercial usage [17-21]. This necessitates the search and exploration of cheap, earth-abundant and highly active electrocatalysts, including carbon-based materials anchored with transition metal nanoalloys, for sustainable and large-scale applications.

N-containing carbon nanostructures are widely used as photocatalysts for green H_2 production because of their excellent stability, abundant surface, molecular structures and porous merits, low-cost and readily available precursors for easy scale-up. [22,23] However, their bandgap (~2.7 eV) and low electrical conductivity limit their utilization as electrocatalysts for water electrolysis [24-26]. The modification of the physicochemical features of N-containing carbon nanostructures by doping with transition metals or alloys could significantly boost its HER electrocatalysis, proved by experimental and theoretical calculations [27-30]. For instance, atomically doped M on 1D N-containing carbon (M/g-C_3N_4, M = Cu, Mn, Fe) delivered superior photo/electrochemical HER activity and stability to pristine g-C_3N_4 because the metal doping

* Corresponding authors.
E-mail addresses: ak.ipadeola@qu.edu.qa (A.K. Ipadeola), kenneth.ozoemena@wits.ac.za (K.I. Ozoemena), bakr@qu.edu.qa (A.M. Abdullah).

https://doi.org/10.1016/j.electacta.2024.145236
Received 11 May 2024; Received in revised form 6 October 2024; Accepted 16 October 2024
Available online 18 October 2024
0013-4686/© 2024 The Authors. Published by Elsevier Ltd. This is an open access article under the CC BY license (http://creativecommons.org/licenses/by/4.0/).

enabled well defined pore sizes, morphology, surface area and accessible active sites [31]. Also, Mo, S co-doping of N-containing carbon (Mo-S-CN) modified its structural architectures for enhanced HER activity relative to the pristine CN, owing to the lowered electron density of Mo center by N-atom for easy Mo-H_2O complex formation, but increased by S for facile H—O bond cleavage and adsorbed H_2O dissociation [32]. Indeed, the incorporation of transition metals, oxides, nitrides and phosphides into the N-containing carbon nanostructures apparently increased their electrocatalysis.

Recently, transition metal phosphides (TMPs) emerged as advanced materials for HER and OER because of their exclusively tailored spherical crystal structures and crystalline surfaces with metal atoms located in the tri-prism and P atoms at the internal void that enables exposure of unsaturated coordination surface atoms (i.e., active sites). Coupled with the moderate electronegativity of P that facilitates optimized binding strength with water electrolytic intermediates, advantageous for boosted HER and OER electrocatalysis [33,34]. Despite the amazing physicochemical merits of the TMPs, the electrocatalytic performance of unary transition metal phosphides (UTMPs) is still far from those of noble-metal-based electrocatalysts. However, HER and OER electrocatalysis of binary transition metal phosphides (BTMPs) were comparable to Pt-based electrocatalysts [35-37]. The BTMPs electrocatalysts are endowed with modifiable electronic properties, heterostructures, and synergism, which are beneficial for HER and OER, with better performance than the UTMP counterparts. For instance, the CoNiP had higher H_2 production rate that was 1.43- and 1.55-folds of Ni_2P and CoP, respectively, attributable to its improved metallic nature, increased conductivity, free electron mobility and modified ᴅ-band center, proven by experimental and theoretical data [38]. Metal-organic framework (MOF)-template synthesis of $Co_xFe_{1-x}P$ nanocubes gave excellent HER activity at lower η_{10} compared to CoP and FeP nanotubes, due to their well-defined crystal structures and synergistic effect of the active sites with electron donating nature [39]. Taking advantages of the physicochemical and electrocatalytic merits of both N-containing carbon and BTMP, the incorporation of BTMP on conductive materials (i.e., carbon and/or nickel foam (NF)) allows easy dispersion/stabilization, eschew agglomeration, augment electrical conductivity and thermal stability that further enhance its bifunctional water electrocatalysis [40-42]. Unlike previous report on the demonstration of NiCoP nanosheets coated NF (NiCoP/NF@NC) at high metal contents for good HER and OER electrocatalysis, due to the synergy among NiCoP, NF and NC [43], but failed to present the performance of NF alone, as NF is highly active electrocatalyst and contributed to the metal loading. An attempt to significantly lower the metal content informed the fabrication of N-containing carbon sheets (NCS) atomically doped NiP-CoP nanohybrid (NiP-CoP/NCS, at ~2.5 wt.%) for improved HER and OER electrocatalysis, which is yet to be reported, as far as we found.

In this work, the rational preparation of NCS atomically doped NiP-CoP nanohybrid (NiP-CoP /NCS) by precipitation and calcination methods for HER and OER electrocatalysis. This is constructed by the complexation of the binary metal (Ni and Co) salts with urea (nitrogen source) and dibasic phosphate salt in a mixture of water and ethanol at 60 °C for 1 h to afford precipitates, which were spread on activated tissue paper (ATP), dried, and annealed at 500 °C for 2 h in N_2 atmosphere. This enables the dispersion of NiP-CoP nanohybrid at low metal contents (~2.5 wt.%) on NCS (sourced from urea and ATP) with tunable physicochemical merits (i.e., downshifted ᴅ-band center, more defects, lower interplanar distance, lattice contraction, induced strains and decreased crystallite size). This synthesis method is facile, reproducible, without hazardous chemicals, and usable for large-scale production. The surface compositions and structural properties of the NiP-CoP/NCS are investigated by various bulk and surface physical characterizations, and its experimental and theoretical HER/OER activities compared to CoP/NCS and NiP/NCS. The influence of electrolytes for green H_2 production was verified, hence, HER was studied in 0.5 M $HClO_4$ and 1.0 M KOH solutions, while OER was probed only in 1.0 M KOH solution.

2. Materials and methods

2.1. Materials

Cobalt (ii) chloride ($CoCl_2$, ≥ 99.90%), nickel(ii) chloride ($NiCl_2$, ≥ 99.90%), potassium phosphate dibasic (K_2HPO_4, ≥ 99.95%), urea ($(NH_2)_2CO$, 99.00–100.50%), hydrochloric acid (HCl, ≥ 37.00%), perchloric acid ($HClO_4$, 70.00%), potassium hydroxide (KOH, ≥ 85.00%) and absolute ethanol (≥ 99.80%) were bought from Sigma Aldrich. Ultrapure water and tissue paper (TP).

2.2. Synthesis of NiP-CoP/NCS, CoP/NCS and NiP/NCS nanostructures

The NiP-CoP/NCS was prepared by low-temperature precipitation and calcination methods. Briefly, $CoCl_2$ (0.05 g), $NiCl_2$ (0.05 g), K_2HPO_4 (0.1 g) and Urea (2.0 g) were added to a solution containing H_2O (5 mL) and ethanol (15 mL), and then stirred vigorously for 1 h at 60 °C to precipitate NiP-CoP/NC. Activated tissue paper (ATP, 2 cm x 8 cm) was initially made by soaking tissue paper (TP) in HCl (3.0 M) for 1 h to remove impurities, then washed with ultrapure water severally and dried at 60 °C for 2 h. Then, the as-formed NiP-CoP/NC precipitates were spread on the ATP and dried at 60 °C in a vacuum oven. The dried NiP-CoP/NC on ATP was further calcined at 500 °C in the flow of N_2 atmosphere at 5 °C/min for 2 h and cooled to room temperature to afford NiP-CoP/NCS. The as-obtained NiP-CoP/NCS was washed severally with ethanol and dried in vacuum oven at 60 °C for 5 h, and then grinded in agape mortar prior to storing for further use. A similar procedure was used for the preparation of CoP/NCS and NiP/CNS using only one metal precursor of $CoCl_2$ (0.1 g) and $NiCl_2$ (0.1 g), respectively.

2.3. Materials characterization

The as-obtained NiP-CoP/NCS nanohybrids were characterized and studied by a scanning electron microscope ((SEM), Hitachi S-4800, Hitachi, Tokyo, Japan) equipped with Energy Dispersive X-Ray Analyzer (EDX) and a transmission electron microscope (TEM, TecnaiG220, FEI, Hillsboro, OR, USA). The X-ray diffraction (XRD) was measured on (X'Pert-Pro MPD, PANalytical Co., Almelo, Netherlands). The X-ray photoelectron spectroscopy (XPS) was carried out on Ultra DLD XPS Kratos, Manchester, UK). The inductively coupled plasma optical emission spectrometry (ICP-OES), Agilent 5800) was performed on (ICP-OES Agilent 5800, USA). Raman spectroscopy was examined by Thermo Scientific Raman instrument.

2.4. Electrochemical HER and OER measurements

The water electrolysis (HER and OER) was performed on Gamry potentiostat (Reference 3000, Gamry Co., Warminster, PA, USA) using the three-electrodes, consisting of Pt wire as a counter, Ag/AgCl as a reference electrode, and electrocatalyst modified glassy carbon (GC) as a working electrode. The ink was prepared by dispersing 2.0 mg of each electrocatalyst in 1.0 mL of aqueous solution of isopropanol/H_2O (3/1 v/v ratio), 50.0 μL of Nafion solution (0.05 wt.%) added and sonicated for 1 h. The uniformly dispersed ink was drop-cast onto the well-polished GC, and dried in a vacuum oven at 60 °C for 1 h. The metal mass loading in the electrocatalysts on the GC was determined as 0.02 ± 0.002 mg/cm^2 by ICP-OES. The HER measurements were carried out in 0.5 M $HClO_4$ and 1.0 M KOH, whereas OER was done in 1.0 M KOH only. Prior to all measurements, the electrolytes were purged with N_2 to remove any dissolved O_2, and the electrocatalysts modified GC were activated and conditioned at 200 mV/s for 50 cycles before the actual measurements. Also, the reference electrode is placed in Luggin capillary and dipped very close to working electrode to mitigate ohmic drop and the Gamry potentiostat is set to automatically correct any uncompensated iR using current interrupt onto the applied signal for HER and

OER measurements. All potentials recorded are referred to reversible hydrogen electrode (RHE) with the formula (RHE = $E_{Ag/AgCl} + E^{o}_{Ag/AgCl}$ + 0.0591 pH), where $E_{Ag/AgCl}$ is the working potential with respect to the reference electrode and $E^{o}_{Ag/AgCl}$ is the standard reduction potential of the reference electrode.

2.5. Theoretical calculations

The density functional theory (DFT) calculations were executed with the supercomputational facilities at the centre for High Performance Computing (CHPC, Cape Town, South Africa), operated at the BIOVIA Material Studio with the adsorption tool location module [44-46]. Various adsorbates (*H) and (*O, *OH and *OOH) were employed to simulate the HER and OER, respectively, on the modelled electrocatalysts with highly exposed active {011} facets, i.e., NiP-CoP{011}, NiP{011} and CoP{011}. The electrocatalysts were modelled with supercells of 3 × 3 layers, then cleaned, and subjected to geometric relaxation calculations at a set threshold energy (10^{-6} eV) and minimal adsorption distance (5 Å) to converge. The DMoI3 was utilized for the estimation of electronic and energy properties at the same threshold energy. The reliability of theoretical calculations was verified by the condensed-phase optimization molecular potential for atomistic simulation studies (COMPASS) force field.

3. Results and discussion

3.1. Physical characterization

The fabrication of NiP-CoP/NCS involves low temperature precipitation and calcination (Fig. 1a). This was based on the chelation of Ni^{2+} and Co^{2+} with HPO_4^{2-} ions and urea in a mixed solution (EtOH/H_2O) at 60 °C for 1 h. The urea serves as source of carbon, nitrogen, and crystalline surface directing agent to the formation of irregular spherical nanoarchitectures of NiP-CoP nanohybrid. Then, the chelated mixture was wrapped with dried activated tissue paper (ATP, i.e., tissue paper previously soaked in 1.0 M HCl for 1 h and predominate the morphology of NCS) and calcinated at 500 °C for 2 h in N_2 atmosphere, which resulted in the formation of NiP-CoP/NCS with spherical-like nanocrystals on sheet-support. This was proved by the SEM image, which reveals broken sheets with anchored ultra-small size nanoparticles for NiP-CoP/NCS (Fig. 1b), whereas NiP/NCS and CoP/NCS have crumpled sheets supported by nanostructures (Figure S1a, S1b). The spherical-like

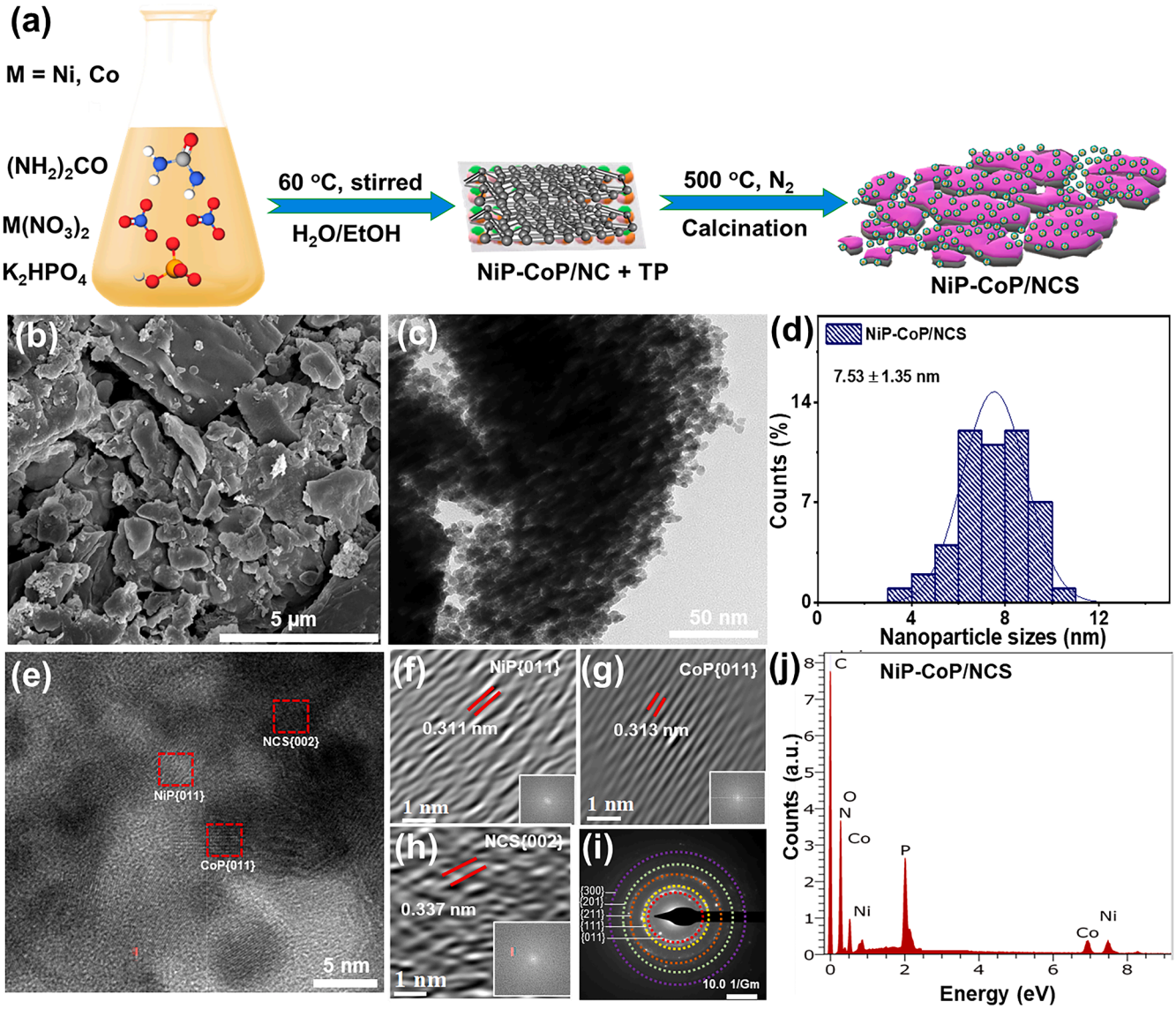


Fig. 1. (a) Synthesis method, (b) SEM, (c) TEM (d) Nanoparticles distribution, (e) HRTEM, (f-h) Fast Fourier transform (FFT) for NiP{011}, CoP{011}, and NCS{002} facets, (i) SAED, and (j) EDX of NiP-CoP/NCS.

nanoarchitectures embedded on nanosheets in NiP-CoP/NCS and NiP/NCS were clearly observed by the TEM images, but amorphous nanostructures were revealed in CoP/NCS (Fig. 1c, S1c, S1d). The nanoparticles were agglomerated in NiP-CoP/NCS, but well-distributed in others with average sizes of 7.53 ± 1.35, 3.28 ± 0.053 and 1.27 ± 0.20 nm for NiP-CoP/NCS, NiP/NCS and CoP/NCS, respectively (Fig. 1d, S1d, S1e). The large nanoparticle sizes of the NiP-CoP/NCS may be traced to the aggregation of NiP and CoP nanoparticles during the calcination. The high-resolution TEM (HRTEM) of NiP-CoP/NCS, NiP/NCS and CoP/NCS showed the lattice fringes with several crystalline defects, including stacking faults, interfacial and intragranular dislocations, indicated by red square box (Fig. 1e, S1g, S1h). The NiP-CoP/NCS has interplanar spacings of 0.311, 0.313 and 0.337 nm for NiP{011}, CoP{011} and NCS {002} facets (Fig. 1f-1h); only NiP{011} and NCS{002} with 0.311 and 0.359 nm estimated in NiP/NCS; and CoP{011} and NCS{002} with 0.315 and 0.359 nm in CoP/NCS. The lower interplanar distance of NCS in NiP-CoP/NCS is attributed to the contractive effect of the binary metal phosphides on the carbon nanosheets lattice. The selected area electron diffraction (SAED) show the predominant diffraction rings of the NiP-CoP/NCS and NiP/NCS ascribable to {011}, {111}, {201}, {211} and {300} facets, which correspond to hexagonal crystal structure of NiP (Fig. 1i, S1i). However, CoP/NCS did not show a clear SAED pattern, due to its amorphous nature, as previously reported [47].

The EDX analysis confirmed the elemental compositions of the electrocatalysts' surfaces: NiP-CoP/NCS (C/N/P/Co/Ni with elemental contents (81.29/12.23/2.96/1.66/1.86 wt.%)); NiP/NCS (C/N/P/Ni with elemental contents (80.11/16.52/1.74/1.64 wt.%)); and CoP/NCS (C/N/P/Co with corresponding elemental contents (69.34/26.91/1.62/2.14 wt.%)) (Fig. 1j, S2a, S2b), as summarized in Table S1. Similarly, the ICP-OES analysis gave only the metal contents of Co/Ni (1.38/1.29 wt.%) in NiP-CoP/NCS, Ni (2.63 wt.%) in NiP/NCS and Co (2.68 wt.%) in CoP/NCS. Although, there is inconsistence in the surface and bulk metal contents by EDX and ICP-OES, respectively, the elemental mapping revealed homogeneous distribution of elements (Ni and/or Co, P, N, C) on the as-prepared NiP-CoP/NCS, NiP/NCS and CoP/NCS (Figure S2c-S2o).

The XRD provides the coexistence and overlap crystalline phases of hexagonal NiP (space group: P-3c1 (#165), $a = b = 1.2311$, $c = 0.4663$) and orthorhombic CoP (space group: Pnma (#62), $a = 0.5670$, $b = 0.3520$, $c = 0.6638$) in NiP-CoP/NCS, only hexagonal NiP in NiP/NCS and orthorhombic CoP in CoP/NCs (Fig. 2a). This confirmed the formation of NiP-CoP nanohybrid, rather than pure NiCoP. Meanwhile, the

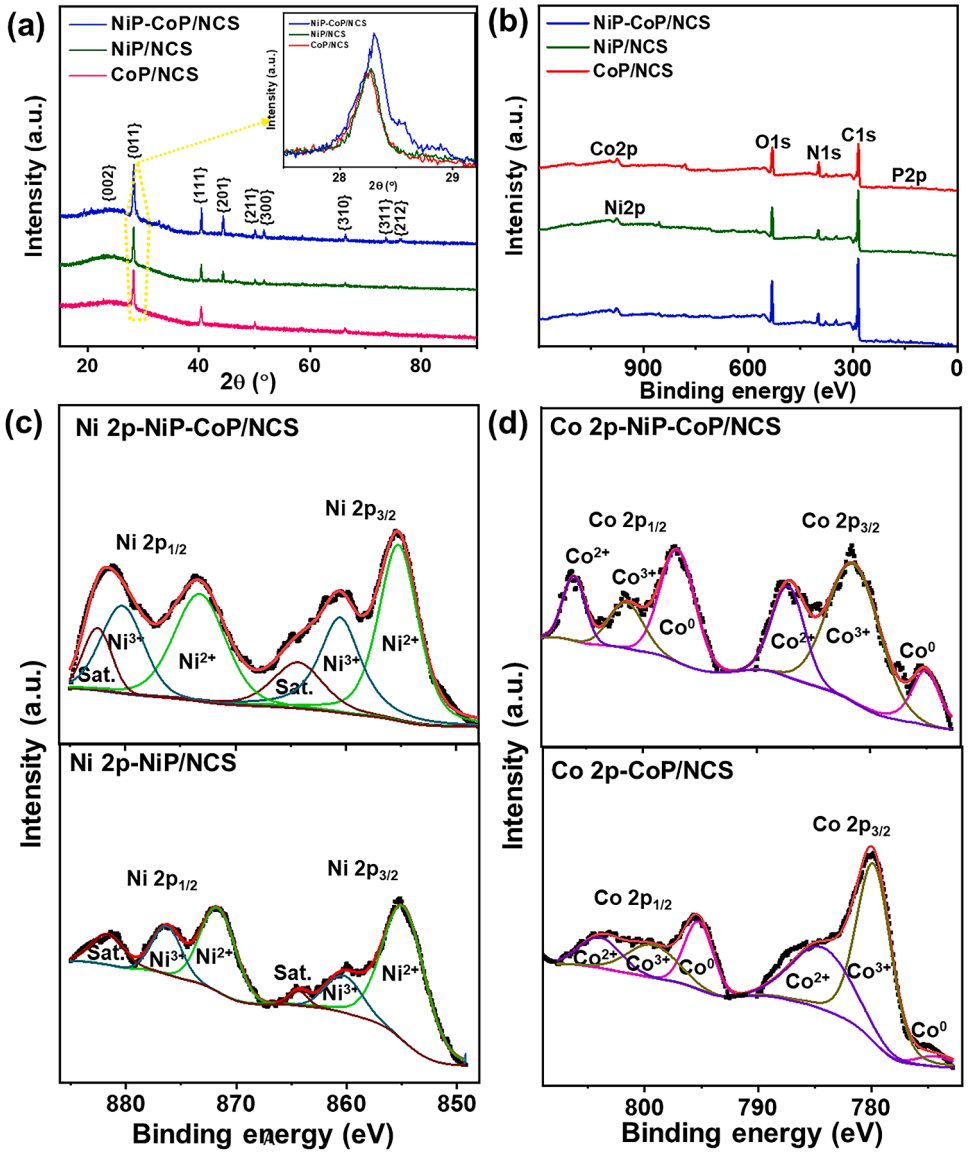


Fig. 2. (a) XRD, (b) XPS survey scan, high-resolution XPS of (c) Ni 2p and (d) Co 2p of NiP-CoP/NCS, NiP/NCS and CoP/NCS.

NiP-CoP/NCS, NiP/NCS and CoP/NCS exhibit respective reference numbers (98–018–2049; 96–153–8448; and 98–002–5726), besides the amorphous phase of graphitic carbon (i.e., NCS) for all the materials. All the materials exhibit broad diffraction of {002} facet assigned to the amorphous carbon sheets (NCS), besides both NiP/NCS and NiP-CoP/NCS have similar diffraction patterns of {011}, {111}, {201}, {211}, {300}, (310}, {311} and {212} facets corresponding to the hexagonal crystal nanostructures. However, CoP/NCS only has diffraction patterns of {011}, {111}, {211}, {310} and {311}, attributed to the orthorhombic crystal structure. There were slight positive shifts of diffraction patterns with higher full width half of maximum (FWHM) in NiP-CoP/NCS, particularly for the most significantly exposed active facet {011}, due to the lattice contraction, induced strains, and decreased crystallite size of the binary metal phosphide. This was further confirmed by the reduced crystallite sizes (23.90 nm), but increased lattice strain ($\varepsilon = 0.00566$) of NiP-CoP/NCS, relative to NiP/NCS (38.33 nm; 0.00388) and CoP/NCS (31.63 nm; 0.00459).

The XPS wide-survey scan shows the presence of core level of C 1 s, N 1 s, P 2p, O 1 s, Ni 2p and/or Co 2p in the materials (Fig. 2b), with the following surface atomic compositions: C (82.88 at.%)/N (11.98 at.%)/P (1.88 at.%)/Ni (1.51 at.%)/Co (1.75 at.%) in NiP-CoP/NCS; C (83.38 at.%)/N (13.65 at.%)/P (1.54 at.%)/Ni (1.43 at.%) in NiP/NCS; and C (80.67 at.%)/N (15.98 at.%)/P (1.70 at.%)/Co (1.65 at.%) in CoP/NCS (Table S1). However, the presence of O 1 s may be traced to the surface oxidation of the materials in air and/or phosphate precursor residue. This agrees with the surface elemental compositions by EDX, but disparate with the bulk metal compositions by ICP-OES analysis, which is an indication of uniform distribution of the elements of the electrocatalysts and advantageous for facile green hydrogen and oxygen production. The binding energies of the high-resolution XPS for each element are summarized in Table S2. The high resolution of the Ni 2p spectra in NiP-CoP/NCS and NiP/NCS shows Ni $2p_{3/2}$ and $2p_{1/2}$ with various oxidation states: Ni^{2+} ($2p_{3/2}$ (855.28 eV) and $2p_{1/2}$ (873.52 eV)), Ni^{3+} ($2p_{3/2}$ (860.60 eV) and $2p_{1/2}$ (880.44 eV)) and satellites phases ($2p_{3/2}$ (864.73 eV) and $2p_{1/2}$ (882.71 eV)) in NiP-CoP/NCS; meanwhile NiP/NCS has Ni^{2+} ($2p_{3/2}$ (855.16 eV) and $2p_{1/2}$ (871.99 eV)), Ni^{3+} ($2p_{3/2}$ (860.58 eV) and $2p_{1/2}$ (878.81 eV)) and satellites phases ($2p_{3/2}$ (864.42 eV) and $2p_{1/2}$ (881.67 eV)) (Fig. 2c). But there were slightly positive shifts in the binding energies of Ni 2p in NiP-CoP/NCS, which implies downshifting of D-band center from the Fermi level on the incorporation of CoP. Similarly, the Co 2p reveals high resolution spectra of Co $2p_{3/2}$ and $2p_{1/2}$ with various oxidation states: Co^0 ($2p_{3/2}$ (775.30 eV) and $2p_{1/2}$ (797.25 eV)), Co^{3+}($2p_{3/2}$ (781.68 eV) and $2p_{1/2}$ (801.44 eV)) and Co^{2+} ($2p_{3/2}$ (787.39 eV) and $2p_{1/2}$ (806.22 eV)) phases in NiP-CoP/NCS; meanwhile CoP/NCS exhibits Co^0 ($2p_{3/2}$ (774.76 eV) and $2p_{1/2}$ (795.46 eV)), Co^{3+}($2p_{3/2}$ (778.87 eV) and $2p_{1/2}$ (799.37 eV)) and Co^{2+} ($2p_{3/2}$ (784.91 eV) and $2p_{1/2}$ (804.06 eV)) phases (Fig. 2d). Also, the integration of NiP in NiP-CoP/NCS downshifted its D-band center for Co 2p from the Fermi level, evidenced by its slightly increased binding energies (Table S2). The P 2p spectra were deconvoluted into three distinct peaks: P $2p_{3/2}$, P $2p_{1/2}$, and PO_4^{3-} for all the samples. This implies that P binds covalently to both the metal atom(s) and C lattice, although there is residue of PO_4^{3-} from the precursor basic phosphate for all the samples (Figure S3a). The C1s spectra of NiP-CoP/NCS, NiP/NCS and CoP/NCS were fitted into three distinct peaks, corresponding to strong C = C, C—C, C—O and weak peaks of C = N bonds (Figure S3b). A small positive shift of the binding energies of C 1 s in NiP-CoP/NCS is observed and attributed to the transfer of more electrons to the binary metal phosphide composite compared to the mono-counterparts (Table S2). Also, the deconvolution of N 1 s spectra give three dissimilar peaks of pyridinic N, pyrrolic N and graphitic N (Figure S3c). which are usually assigned to N-doped carbon materials [48,49]. The high resolution O 1 s spectra of NiP-CoP/NCS, NiP/NCS and CoP/NCS reveal three distinct peaks corresponding to metal adsorbed oxygen (M-O), oxygen vacancy (O_L) and hydroxyl species (˙OH). Thus, the NiP-CoP/NCS is endowed with modulated electronic structures and electrical conductivity, which are beneficial for facile green hydrogen and oxygen production.

The Raman spectra of the NCS in NiP-CoP/NCS, NiP/NCS and CoP/NCS reveal four distinct peaks corresponding to D-, G-, D'- and 2D-bands at respective Raman shifts of 1355.2, 1578.7, 1774.6 and 2844.2 cm^{-1} (Figure S4a). The presence of three defective peaks (D-, D'- and 2D-bands) implies defective sites in the NCS on the incorporation of N- and metal atom(s) in NiP-CoP/NCS, NiP/NCS and CoP/NCS. The extent of defect in NiP-CoP/NCS, NiP/NCS and CoP/NCS is determined by the I_D/I_G ratio, thereby NiP-CoP/NCS has slightly increased I_D/I_G (3.6) than those of NiP/NCS (3.5) and CoP/NCS (3.3). The FTIR spectra of the NiP-CoP/NCS, NiP/NCS and CoP/NCS reveal various vibrational modes of -OH/-NH, C—H, C = C = N, C = N, C—N, and C—O-C groups (Figure S4b), which corroborate the integration of nitrogen atoms in the lattice of NCS and agrees with the XPS results.

The N_2 adsorption/desorption isotherms of the NiP-CoP/NCS, NiP/NCS and CoP/NCS resembles the isotherm type IV, according to International of Pure and Applied Chemistry (IUPAC) classification with H4 hysteresis loop at two steps condensation of $P/P_o \geq 0.2$ and $P/P_o < 1.0$ (Figure S5a). This led to the higher specific surface area (SSA = 55.15 m^2/g) and porosity (0.020 cm^3/g) measured for NiP-CoP/NCS relative to NiP/NCS (22.93 m^2/g; 0.008 cm^3/g) and CoP/NCS (38.56 m^2/g; 0.013 cm^3/g). The increased SSA and porosity of NiP-CoP/NCS were ascribable to its more accessible active sites, which were advantageously utilized for HER and OER electrocatalysis. Meanwhile, mean pore sizes of 8.79, 7.92 and 8.90 nm were measured for NiP-CoP/NCS, NiP/NCS and CoP/NCS, respectively (Figure S5b).

3.2. Hydrogen evolution reaction (HER)

Enthused by the physicochemical merits of the transition metal phosphide composites, the HER activity of the NiP-CoP/NCS, NiP/NCS and CoP/NCS was extensively studies in both acid and alkaline conditions utilizing various electrochemical techniques. The electrochemical behavior of the NiP-CoP/NCS, NiP/NCS and CoP/NCS was investigated in 0.5 M $HClO_4$ solution using cyclic voltammetry (CV) at 20 mV/s and exhibit seemingly pseudo-rectangular signatures at the potential range (0.1 - 0.2 V vs. RHE) (Fig. 3a). These revealed non-faradaic or capacitive behavior of the electrocatalysts, but the charge storage capacity follows a trend of NiP-CoP/NCS > CoP/NCS > NiP/NCS. This translate to higher electrochemical active surface area (ECSA) of the NiP-CoP/NCS, compared to CoP/NCS and NiP/NCS, which were determined using the capacitive method of the CV curves for NiP-CoP/NCS, NiP/NCS, and CoP/NCS at varied scan rates (υ) (Fig. 3b-3d). A plot of $\Delta j/2_{@-0.15\ V}$ against υ, whose slope was used to calculate the ECSA of the electrocatalysts in 0.5 M $HClO_4$ solution (Fig. 3e). Hence, the ECSA of NiP-CoP/NCS (38.7 m^2/g) is 1.83- and 4.07- folds of and CoP/NCS (21.1 m^2/g) and NiP/NCS (9.5 m^2/g) respectively (Fig. 3f), which has similar trend of specific surface area obtained for the BET analysis. The increased ECSA of the NiP-CoP/NCS is ascribed to its modulated physicochemical merits, including downshifted D-band center, more defects, lower interplanar distance, lattice contraction, induced strains, decreased crystallite size, increased SSA and porosity. These unique physicochemical merits of the NiP-CoP/NCS are beneficially utilized for enhanced HER and OER electrocatalysis.

The HER polarization curves of electrocatalysts in 0.5 M $HClO_4$ solution show that the NiP-CoP/NCS exhibits higher HER performance than NiP/NCS, CoP/NCS and NCS (Fig. 4a). This is proved by the lower overpotential at benchmarked 10 mA/cm^2 (η_{10} = 197.7 mV) of NiP-CoP/NCS relative to NiP/NCS (397.9 mV), CoP/NCS (408.6 mV) and NCS (not reached 10 mA/cm^2) (Fig. 4b). This is an indication that NiP-CoP/NCS required lower energy to produce green H_2 in $HClO_4$ solution relative to NiP/NCS and CoP/NCS. The η_{10} of NiP-CoP/NCS (197.7 mV) is superior to previously reported metal-doped N-containing carbon nanostructures in the literature, including 0.12Cu-C_3N_4 (390.0 mV) [50], Co@NC (230 mV) [51], Cu/g-C_3N_4 (449.0 mV) [31],

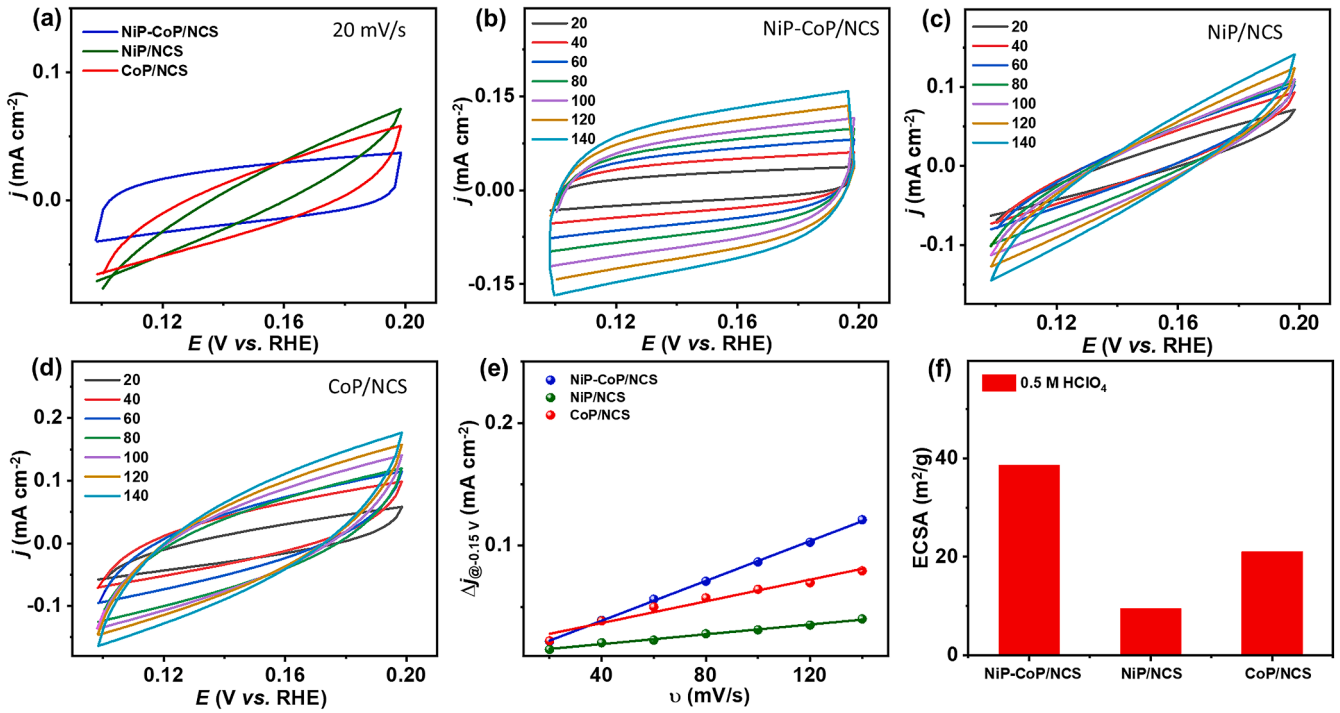


Fig. 3. (a) Comparative CV curves of the electrocatalysts at 20 mV/s, CV curves at varied scan rates (υ) (b) NiP-CoP/NCS, (c) NiP/NCS, (d) CoP/NCS, (e) Plots of $\Delta j/2_{@-0.15\ V}$ vs. υ and (f) ECSA of NiP-CoP/NCS, NiP/NCS, and CoP/NCS in 0.5 M $HClO_4$ solution.

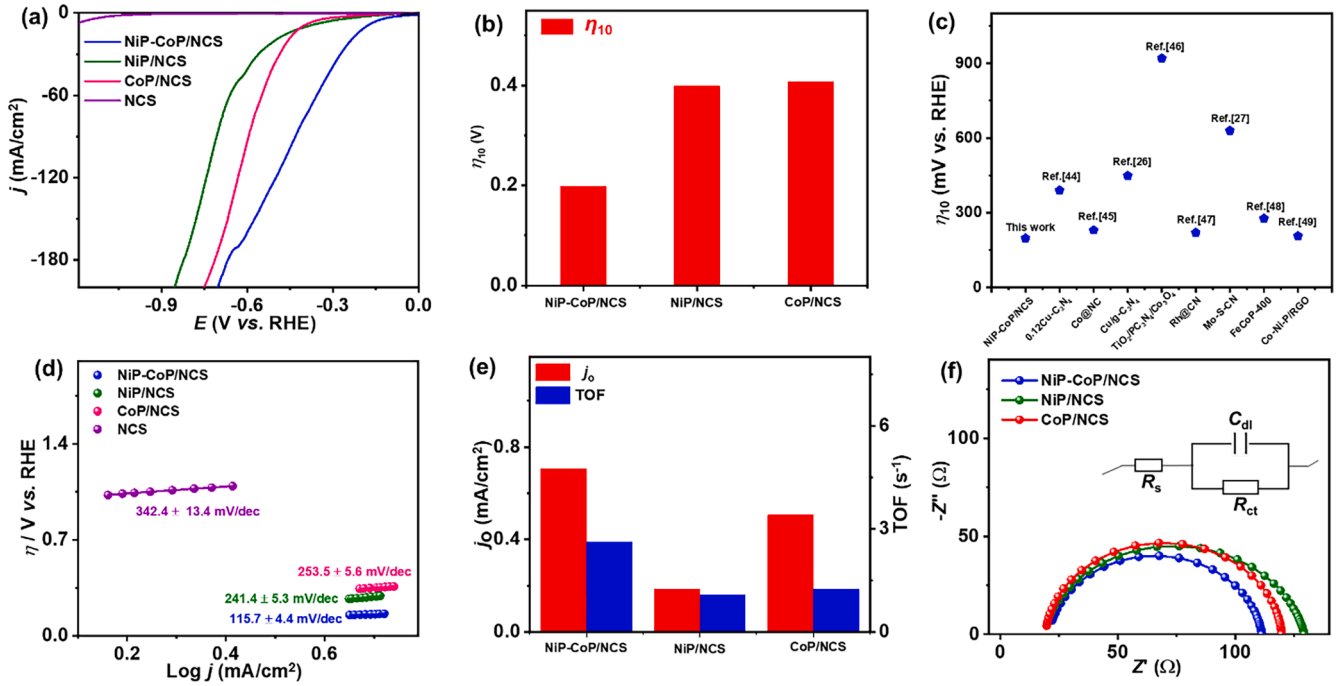


Fig. 4. (a) Comparative HER polarization curves of the electrocatalysts at 2 mV/s, (b) η_{10}, (c) Comparative η_{10} with literature, (d) Tafel plots, (e) j_o and TOF, (f) Nyquist plots at −0.197 V with Voigt electrical equivalent circuit (EEC, inset) of NiP-CoP/NCS, NiP/NCS, and CoP/NCS in 0.5 M $HClO_4$ solution.

$TiO_2/PC_3N_4/Co_3O_4$ (920.0 mV) [52], Rh@g-CN (220.0 mV) [53], Mo-S-CN (630.0 mV) [32], Fe-Co-P-400 (277.0 mV) [54], Co-Ni-P/RGO (207.0 mV) [55] (Fig. 4c), and others in Table S3. The Tafel plots of the electrocatalysts in 0.5 M $HClO_4$ solution reveal lower Tafel slope (b_c = 115.7 ± 4.4 mV/dec) for NiP-CoP/NCS than NiP/NCS (241.4 ± 5.3 mV/dec), CoP/NCS (253.5 ± 5.6 mV/dec) and NCS (342.4 ± 13.4 mV/dec) (Fig. 4d). This implies that the tuned physicochemical merits of NiP-CoP/NCS enable the HER mechanism in 0.5 M $HClO_4$ to proceeds via the Volmer-Heyrovsky reactions, including H_2O activation and dissociation in the $HClO_4$ solution (i.e., $H_2O \rightarrow H^+ + OH^-$), then adsorption of proton on the electrocatalyst's active sites (M*) (i.e., $H^+ + M^* + e^- \rightarrow M^*H_{ads}$) and finally recombination of the protons (i.e., $M^*H_{ads} + H^+ + e^- \rightarrow H_2 + M^*$) [17,18]. Also, the NiP-CoP/NCS displayed superior HER activity and kinetics in the $HClO_4$ solution, evidenced by its

increase exchange current density (j_o = 0.7066 mA/cm^2), turn-over frequency (TOF = 2.63 s^{-1}) and H_2 production rate (3601.63 μmol/g/h) relative to NiP/NCS (0.1846 mA/cm^2; 1.07 s^{-1}; 2701.22 μmol/g/h), CoP/NCS (0.5054 mA/cm^2; 1.25 s^{-1}; 2881.31 μmol/g/h) and NCS (0.0520 mA/cm^2, 0.0005 s^{-1}; 23.52 μmol/g/h) (Fig. 4e, S6). Despite the importance of these parameters of indicator for HER electrocatalysis, literature rarely reports the j_o, TOF and H_2 production rate for metal-doped N-containing carbon nanostructures. Nevertheless, the j_o of NiP-CoP/NCS (0.7066 mA/cm^2) is higher than few reports in the literature, like Mo-S-CN (0.29 mA/cm^2)[32], and Co-Ni-P/RGO (0.0004 mA/cm^2)[55] (Table S3). The excellent HER performance of NiP-CoP/NCS is attributed to its compositional synergism and tuned physicochemical features.

The HER kinetics are further probed by the electrochemical impedance spectroscopy (EIS) to infer the interfacial electrode-electrolyte behavior. The Nyquist plots of the NiP-CoP/NCS, NiP/NCS, and CoP/NCS in 0.5 M $HClO_4$ solution displays a semi-circle signature in the trend of NiP-CoP/NCS < CoP/NCS < NiP/NCS (Fig. 4f), which was modelled with Voigt electrical equivalent circuit (EEC, Fig. 4f inset) to extract the EIS data, as summarized in Table 1. Three distinct EIS parameters were obtained, including the solution resistance (R_s), charge transfer resistance (R_{ct}) and double-layer capacitance (C_{dl}). The R_s of NiP-CoP/NCS, NiP/NCS and CoP/NCS are the same within the confinement of error bars, implying similar electrolyte resistivity for all the electrocatalysts during the HER in 0.5 M $HClO_4$ solution. However, the R_{ct} decreased in the order of NiP-CoP/NCS (90.74 ± 0.66 Ω) < CoP/NCS (100.60 ± 0.61 Ω) < NiP/NCS (111.50 ± 0.78 Ω) revealed that NiP-CoP/NCS has better HER kinetics, which agrees with the HER polarization curves. The charge storage capacity (C_{dl}) of the NiP-CoP/NCS (0.909 ± 0.066 μF) is also superior to those of CoP/NCS (0.67 ± 0.059 μF) and NiP/NCS (0.883 ± 0.089 μF). This is traced to the ease of ions and electron mobility in NiP-CoP/NCS during HER electrocatalysis in 0.5 M $HClO_4$ solution compared to the mono-metallic analogues [56].

The chronopotentiometry (CP) of the NiP-CoP/NCS, NiP/NCS and CoP/NCS at 10 mA/cm^2 in 0.5 M $HClO_4$ solution for 24 h revealed a low overpotential for NiP-CoP/NCS (201.3 mV), followed by CoP/NCS (404.6 mV) and then NiP/NCS (410.2 mV) (Fig. 5a). This implies that enhanced green H_2 production in $HClO_4$ requires low energy in the following trend of NiP-CoP/NCS < CoP/NCS < NiP/NCS. The HER polarization curves after the 24 h stability show that all the electrocatalysts degrade, proved by increase in their overpotentials (η_{10}/η_{100}) after CP test by 14.6/20.3 mV, 32.2/31.4 mV and 42.3/38.4 mV for NiP-CoP/NCS, NiP/NCS and CoP/NCS, respectively (Fig. 5c-5d). This indicates that the HER stability on NiP-CoP/NCS was the most stable in 0.5 M $HClO_4$ solution, due to its robust lattice contraction, rich defect and modulated electronic structures. Hence, the structural morphology of the electrocatalysts were retained after the CP stability tests (Figure S7).

Akin to the HER activity of the electrocatalysts in acidic condition, their performance was also probed in alkaline medium (1.0 M KOH). The CV curves of the NiP-CoP/NCS, NiP/NCS, and CoP/NCS in 1.0 M KOH solution at 20 mV/s displayed quasi-rectangular voltammograms (Figure S8a). The electrochemical behavior of the electrocatalysts in 1.0 M KOH electrolytes at a capacitive region (0.1 – 0.2 V vs. RHE) with NiP-CoP/NCS having a higher charge storage ability, followed by CoP/NCS and then NiP/NCS. At varied scan rate, the voltammograms' shapes are retained with increasing current density for all electrocatalysts (Figure S8b-S8d). Hence, the (ECSA) of the NiP-CoP/NCS (57.1 m^2/g) is 2.44- and 2.27-times those of NiP/NCS (23.4 m^2/g) and CoP/NCS (25.1 m^2/g), calculated from the slope of the plots of $\Delta j/2_{@-0.15\ V}$ against υ (Figure S8e, S8f). Notably, the ECSA of all the electrocatalysts are higher in 1.0 M KOH than in 0.5 M $HClO_4$, may be due to the abundance of OH^- ions in KOH, which is not detrimental to poisoning the electrocatalysts' active sites, unlike Cl^- ions in $HClO_4$. The HER polarization curves of electrocatalysts in 1.0 M KOH solution reveals better higher HER activity on NiP-CoP/NCS with respect to lower η_{10} (274.6 mV) compared to NiP/NCS (475.6 mV) and CoP/NCS (398.0 mV) (Figure S9a, S9b). This implies better alkaline HER activity on NiP-CoP/NCS relative to the mono-metallic phosphide composites. The Tafel plots of the electrocatalysts in alkaline medium revealed lower b_c (27.56 ± 3.60 mV/dec) for NiP-CoP/NCS relative to NiP/NCS (62.65 ± 3.08 mV/dec) and CoP/NCS (51.33 ± 2.76 mV/dec) (Figure S9c, S9d). Interestingly, this result shows that Volmer-Tafel mechanism predominates for the alkaline HER electrocatalysis on the NiP-CoP/NCS, which involves activation/dissociation of water ($H_2O \rightarrow H^+ + OH^-$) in KOH electrolyte, adsorption/binding of protons to the M* ($M^* + H^+ + e^- \rightarrow M^*H_{ads}$) and recombination of desorbed protons ($M^*H_{ads} + M^*H_{ads} \rightarrow H_2 + 2M^*$). Moreover, the NiP-CoP/NCS exhibits higher HER activity and kinetics in alkaline medium with respect to superior j_o =(0.6746 mA/cm^2), TOF (1.47 s^{-1}) and H_2 production rate (2519.12 μmol/g/h) compared to NiP/NCS (0.5407 mA/cm^2; 0.64 s^{-1}; 2141.25 μmol/g/h), and CoP/NCS (0.6618 mA/cm^2; 0.78 s^{-1}; 2015.30 μmol/g/h) (Figure S6). Thus, NiP-CoP/NCS has the best capability for generating high purity green H_2 in alkaline medium.

The Nyquist plots of the NiP-CoP/NCS, NiP/NCS and CoP/NCS during the alkaline HER display two distinct deformed semi-circles, i.e., double capacitive loops: one at high frequency region (i.e., 0 – 20 Ω on the horizontal axis (Z^I)) and the other at low frequency region (i.e., > 20 Ω on the horizontal axis (Z^I)) (Figure S9e), which are appropriately modelled with Voigt EEC of 2RC (Figure S9f, inset) to obtain the EIS data, as highlighted in Table S4. For HER in KOH solution, 2RC circuits were utilized with the first RC circuit corresponding to a thin film formation with circuit elements of thin film resistance (R_f) and constant phase elements (CPE_1), while the second RC circuit represents the electrocatalyst-electrolyte interface with circuit elements of R_{ct} and CPE_2, in addition to R_s. The CPEs are appropriate to define the two deformed semi-circles of the Nyquist plots. All the electrocatalysts have almost similar (R_s ~5.0 Ω) within the confinement of error bars, suggesting the same electrolyte resistivity for all the electrocatalysts in alkaline condition during HER electrocatalysis. However, the sum of ($R_f + R_{ct2}$) decreased in the trend NiP-CoP/NCS (25.32 ± 0.76 Ω) < CoP/NCS (239.86 ± 4.28 Ω) < NiP/NCS (258.14 ± 4.55 Ω), indicates improved HER kinetics on NiP-CoP/NCS. However, the total charge storage capacity ($CPE_1 + CPE_2$) increased in the order of NiP-CoP/NCS > CoP/NCS > NiP/NCS, revealed more rapid charge/electron mobility of the NiP-CoP/NCS that facilitates easy adsorption of HER intermediates and fast HER kinetics, compared to CoP/NCS and NiP/NCS. However, closeness of the ideality factors (n_1 and n_2) to 0.5 for NiP/NCS, amongst others, indicates increased electrolyte diffusion. The CP test of the NiP-CoP/NCS at 10 mA/cm^{-2} in 1.0 M KOH solution for 24 h reveals its superior stability requiring lower overpotential for green H_2 production, relative to CoP/NCS and NiP/NCS (Figure S10a). The extent of degradation follows a pattern of NiP/NCS > CoP/NCS > NiP-CoP/NCS, implying that NiP-CoP/NCS is the most stable for alkaline H_2 production. Then, HER activity of the electrocatalysts after the CP test for 24 h stability show an increase in the η_{10} by 17.7 mV, 58.1 mV and 21.8 mV for NiP-CoP/NCS, NiP/NCS and CoP/NCS, respectively (Figure S10b-S10d). This result reveals that NiP-CoP/NCS still retains higher alkaline HER activity after the 24 h stability test than the unary metal phosphides counterparts.

Table 1
EIS data for HER electrocatalysis in 0.5 M $HClO_4$ solution.

	R_s (Ω)	R_{ct} (Ω)	C_{dl} (uF)
NiP-CoP/NCS	20.04 ± 0.47	90.74 ± 0.66	0.909 ± 0.066
NiP/NCS	19.97 ± 0.46	111.50 ± 0.78	0.883 ± 0.089
CoP/NCS	19.31 ± 0.28	100.60 ± 0.61	0.67 ± 0.059

3.3. Oxygen evolution reaction (OER)

The OER activity of the electrocatalysts was probed only in alkaline condition. The OER polarization curves of the NiP-CoP/NCS, NiP/NCS and CoP/NCS at 2 mV/s in 1.0 M KOH solution reveals lower η_{10} (309.1

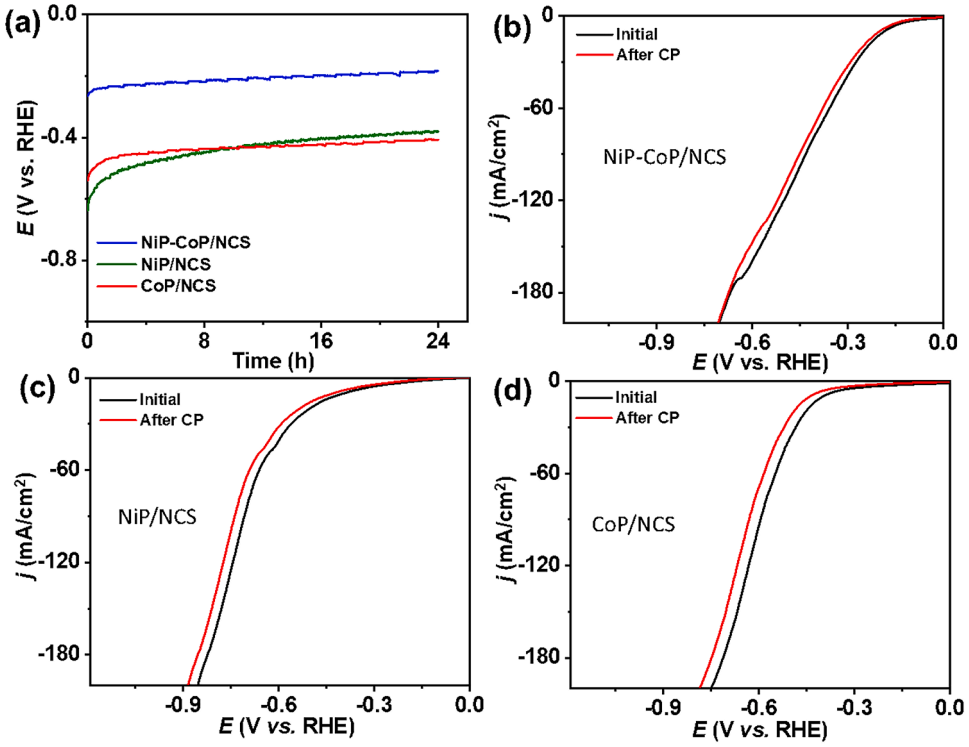


Fig. 5. (a) Chronopotentiometry (CP) plots at 10 mA/cm^2, HER polarization curves at 2 mV/s before and after CP of (b) NiP-CoP/NCS, (c) NiP/NCS, and (d) CoP/NCS in 0.5 M $HClO_4$ solution.

mV) for NiP-CoP/NCS than those of NiP/NCS (360.5 mV) and CoP/NCS (355.8 mV) (Figure S11a, S11b). This implies facile O_2 production on NiP-CoP/NCS relative to other electrocatalysts studied. The OER kinetics are further verified by the Tafel plots with regards to decreased anodic Tafel slope (b_a) in the order of NiP-CoP/NCS (58.9 ± 3.0 mV/dec) < NiP/NCS (63.8 ± 1.3 mV/dec) < CoP/NCS (65.1 ± 1.4 mV/dec) (Figure S11c). Hence, the NiP-CoP/NCS has the best OER kinetics, amongst the studied electrocatalysts. Also, the OER kinetics of NiP-CoP/NCS is better than many reports in the literature, in term of lower η_{10}/b_a values (309.1 mV/58.9 mV/dec) relative to NiCoP CF (370.0 mV/60.7 mV/dec) [57], N-FeCoP (327.0 mV/84.0 mV/dec) [58], MnP-400 (313.0 mV/106.0 mV/dec) [59], NiFeP@NPC (350.0 mV/78.0 mV/dec) [60], Ni-Co-P (318.0 mV/92.7 mV/dec) [61], $Fe_{1.1}Mn_{0.9}P$ (440.0 mV/53.0 mV/dec), Fe_3CoP_xO (430.0 mV/143.0 mV/dec) [62], and NiCo-TEP-400 (310.0 mV/68.0 mV/dec) [63] (Figure S11d, Table S5). The intrinsic OER activity of the electrocatalysts were further examined by the TOF and O_2 production rate with higher values recorded for NiP-CoP/NCS (3.67 s^{-1}; 3643.96 μmol/g/h) than CoP/NCS (1.96 s^{-1}; 3120.74 μmol/g/h) and NiP/NCS (1.59 s^{-1}; 2453.55 μmol/g/h) (Figure S11e). The NiP-CoP/NCS has the best O_2 production rate, ascribable to its modulated physicochemical merits (i.e., lower interplanar spacing and crystallite size, lattice contraction, induced strains, defects, and downshifted ᴅ-band center). The Nyquist plots of the NiP-CoP/NCS, NiP/NCS, CoP/NCS and Pt/C during OER show two semi-circles (Figure S11f), which were fitted with Voigt EEC to acquire the EIS parameters, as expressed in Table S6. The two semi-circles represent 2RC circuits for OER in alkaline solution: the first RC circuit corresponds to a thin film formation with circuit elements of R_f and C_{dl1}, while the second RC circuit is the electrocatalyst-electrolyte interface with circuit elements of R_{ct} and C_{dl_2}, besides R_s. Lower R_s (3.72 ± 0.16 Ω) was recorded for NiP-CoP/NCS compared to NiP/NCS (4.81 ± 0.34 Ω) and CoP/NCS (4.85 ± 0.34 Ω). This is an indication that the electrolyte resistivity of the electrocatalysts decrease during the OER in the order of NiP-CoP/NCS < NiP/NCS < CoP/NCS. This may be traced to increased active sites of the electrocatalysts as proved by the TOF. Nevertheless, the ($R_f + R_{ct}$) decreased as NiP-CoP/NCS (53.03 ± 3.25 Ω) < CoP/NCS (103.41 ± 2.41 Ω) < NiP/NCS (116.91 ± 3.15 Ω), confirmed the superior kinetics and O_2 production rate on NiP-CoP/NCS, amongst the electrocatalysts. Similarly, the NiP-CoP/NCS displays higher ($C_{dl1} + C_{dl2}$) (526.49 ± 5.63 μF) compared to CoP/NCS (422.07 ± 11.92 μF) and NiP/NCS (393.59 ± 5.92 μF), which may be traces to optimized adsorption of OER intermediates on the active sites of the NiP-CoP/NCS and may enable easy charge/electron transport.

The chronoamperometry (CA) of the electrocatalysts toward OER at 1.54 V shows that NiP-CoP/NCS retained the high j (10.24 mA/cm^2) after 24 h, compared to CoP/NCS (1.88 mA/cm^2) and NiP/NCS (1.67 mA/cm^2) (Figure S12a). This infers the excellent OER stability on NiP-CoP/NCS, amongst others. The degree of degradation of the electrocatalysts toward OER after 24 h stability, with respect to increased η_{10} after CA test with small gap are in the trend of NiP-CoP/NCS (14.6 mV) < CoP/NCS (22.2 mV) < NiP/NCS (45.7/mV), shown by the comparative OER polarization curves before and after CA test (Figure S12b-S12d), which further corroborates the impressive OER stability of NiP-CoP/NCS, due to its augmented crystallinity and electronic architectures. The retention of the chemical natures of the spent electrocatalysts after OER stability was confirmed with the high resolution XPS for Ni 2p, Co 2p, P 2p and O 1 s of all the spent electrocatalysts (Figure S13). However, the binding energies Ni 2p shifted to lower values resulted in the formation of main Ni^0 $2p_{3/2}$ (852.60 eV), Ni^0 $2p_{1/2}$ (869.95 eV), $Ni^{2+}2p_{3/2}$ (856.05 eV), Ni^{2+} $2p_{1/2}$ (873.85 eV) and satellites phases ($2p_{1/2}$ (861.59 eV) and $2p_{1/2}$ (880.48 eV)), but those of Co 2p shifted to higher values with the formation of Co^{3+} $2p_{3/2}$ (781.31 eV), Co^{3+} $2p_{1/2}$ (796.36 eV), Co^{2+} $2p_{3/2}$ (785.65 eV), Co^{2+} $2p_{1/2}$ (800.06 eV) and satellites phases ($2p_{3/2}$ (789.59 eV) and $2p_{1/2}$ (804.42 eV)) in NiP-CoP/NCS after OER, rather than the formation of Ni 2p (containing Ni^{2+}, Ni^{3+}, and satellite) and Co 2p (containing Co^0, Co^{3+} and Co^{2+}) in the as-prepared electrocatalysts (Fig. 2c,d, Table S2). This is evidenced that after OER only Co oxide active species are formed, but more metallic Ni active species are presence in the electrocatalysts, besides the adsorption of oxygenated species on the electrocatalysts' surfaces from the residue

phosphate.

3.4. Theoretical simulations

The DFT calculations were utilized to simulate the HER and OER electrocatalysis with proposed intermediate species as adsorbates (*H, *O, *OH and *OOH) on the most significantly exposed {011} facets of NiP-CoP, NiP and CoP surfaces' model, evidenced by the XRD (Fig. 2a), where the adsorption energy (A.E) range was set at 100 kcal/mol with energy difference (0 kcal/mol), defined as ($E_{surface+absorbate} - (E_{surface} + E_{adsorbate}$). The theoretical data of the physical properties of the electrocatalysts with and without the absorbates are summarized in Table 2. In the simulated HER, a lower adsorption energy of H* on NiP-CoP{011} (−0.4874 kcal/mol) compared to NiP{011} (−0.7678 kcal/mol) and CoP{011} surfaces (−0.5169 kcal/mol), implying moderate adsorption of H* on NiP-CoP{011} that is beneficial for rapid desorption and recombination for excellent H_2 production[64], relative to NiP{011}r and CoP{011}. This was traced to the synergistic effect of binary metal phosphide for improved HER electrocatalysis on NiP-CoP{011} and corroborates the experimental data. Also, the adsorbates (*O, *OH and *OOH) were used to simulate the OER on NiP-CoP{011}, NiP{011} and CoP{011} with respective adsorption energies (−0.5951, −0.8509 and −30.3684 kcal/mol), (−1.0168, −1.4256 and −20.0492 kcal/mol) and (−0.6121, −0.7858 and −30.8442 kcal/mol). The results proved the enhanced OER electrocatalysis on the NiP-CoP{011} compared to NiP {011} and CoP{011}, particularly for *O and *OH adsorbates, due to the synergy of co-existed NiP and CoP, and aligned with the experimental data. However, the extremely large energy of *OOH on the electrocatalysts' surfaces showed that it is the slowest reaction step, i.e., potential determining step (p.d.s.) during the OER electrocatalysis with optimized energy recorded on the NiP-CoP{011}, amongst others.

Similarly, the reaction pathways for the adsorbates (*H, *O, *OH and *OOH) on the electrocatalysts' surfaces simulated for HER and OER electrocatalysis (Fig. 6). Notably, the Gibbs free energy (F.E.) of −0.49, −0.77 and 0.517 kcal/mol were recorded for the adsorption of H* on NiP-CoP{011}, NiP{011} and CoP{011}, respectively. This implies that favorable *H adsorption and its facile desorption/recombination for spontaneous HER [65], predominantly occurred on the active site of NiP-CoP{011}, owing to the synergistic effect, relative to the monometallic counterparts. This confirmed the mechanism of HER on the electrocatalysts, in proton-rich conditions (i.e., acidic media) to proceed via Tafel-Volmer pathway, aligning with experimental data. The reaction pathway of OER with absorbates (O*, *OH and *OOH) on the electrocatalysts, reveal respective Gibbs F.E (−0.60, −0.85 and −30.37 kcal/mol) for NiP-CoP{011}, relative to NiP{011} (−1.02, −1.43 and −20.05 kcal/mol) and CoP{011} (−0.61, −0.79 and −30.84 kcal/mol).

Table 2
Theoretical calculations of the adsorbates (*H) and (*O, *OH, *OOH) for simulating HER and OER on the electrocatalysts (NiP-CoP, NiP and CoP). Adsorption energy (A.E) and Gibbs free energy (FE).

Catalysts	Adsorbates	A.E (kcal/mol)	Gibbs F.E (kcal/mol)
CoP	None		
	*O	−0.6121	−0.6121
	*H	−0.5169	−0.5169
	*OH	−8.8149	−0.7858
	*OOH	−60.4549	−30.8442
NiP	None		
	*O	−1.0168	−1.0168
	*H	−0.7678	−0.7678
	*OH	−9.4547	−1.4256
	*OOH	−49.6599	−20.0492
NiP-CoP	None		
	*O	−0.5951	−0.5951
	*H	−0.4874	−0.4874
	*OH	−8.8800	−0.8509
	*OOH	−8.8800	−30.3684

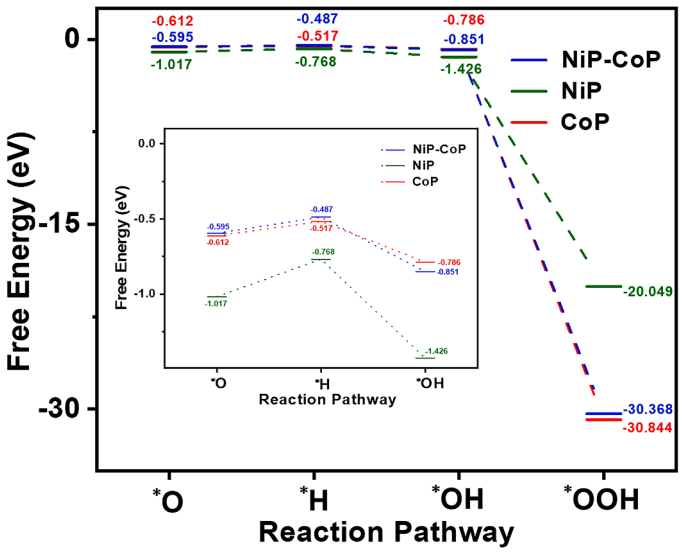


Fig. 6. Reaction coordinates of the absorbates on the electrocatalysts (NiP-CoP {011}, NiP{011} and CoP{011}).

The much lower Gibbs free energy of NiP{011} revealed the best OER spontaneity, amongst the three simulated catalysts, but optimized intermediate species adsorption and rapid desorption for improved OER activity, kinetics and O_2 production rate are confirmed on the NiP-CoP {011}, due to its lowest adsorption energies for the intermediate species. Also, the *OOH adsorption has the highest energy barriers on all the electrocatalysts revealed that it is the potential-determining step (p.d.s) for OER [66]. Hence, the mechanism of OER on NiP-CoP/NCS proceed via a four step pathways, including (i) H_2O dissociation into *OH and H^+, (ii) adsorption of O species (*O), (iii) generation of *OOH and (iv) desorption of *OOH to produce O_2, H_2O and H^+ (p.d.s) [67].

$$H_2O + * \rightarrow *OH + H^+ + e^- \quad \text{(i)}$$

$$*OH + H_2O \rightarrow *O + H_2O + H^+ + e^- \quad \text{(ii)}$$

$$*O + H_2O \rightarrow *OOH + H^+ + e^- \quad \text{(iii)}$$

$$*OOH + H_2O \rightarrow * + O_2 + H_2O + H^+ + e^- \quad \text{(iv)}$$

4. Conclusions

This work presents the rational synthesis of N-containing carbon sheets atomically doped NiP-CoP nanohybrid (NiP-CoP/NCS) by precipitation and calcination method, and its HER and OER were tested experimentally and theoretically. The fabrication mechanism enabled tailored physicochemical merits, including surface area/porosity, downshifted D-band center, interplanar distance, lattice contraction, lower crystallite size, adsorption, and Gibbs free energy, that are highly beneficial for HER and OER electrocatalysis, proven experimentally and theoretically. Hence, the NiP-CoP/NCS exhibited great HER activity at lower η_{10} (197.7/274.6 mV), higher j_o (0.71/0.67 mA/cm^2), TOF (2.63/1.47 s^{-1}) and H_2 production rate (3601.63/2519.12 μmol/g/h) in acid/alkaline media, compared to NiP/NCS (397.9/475.6 mV; 0.18/0.54 mA/cm^2; 1.07/0.64 s^{-1}; 2701.22/2141.25 μmol/g/h) and CoP/NCS (408.6/398.0 mV; 0.51/0.66 mA/cm^2; 1.25/0.78 s^{-1}; 2881.31/2015.30 μmol/g/h), besides impressive HER stability with only small η increase after 24 h CP test. The acidic and alkaline HER mechanisms on NiP-CoP/NCS follow Volmer-Heyrovsky and Volmer-Tafel pathways, respectively. Also, excellent OER activity, kinetics and stability were recorded on NiP-CoP/NCS at lower η_{10} (309.1 mV), b_a (58.9 ± 3.0 mV/dec) and R_{ct1}+R_{ct2} (53.03 ± 3.25 Ω), but increased TOF (3.67 s^{-1}) and O_2 production rate

(3643.96 μmol/g/h) relative to NiP/NCS and CoP/NCS, and retained high j (10.24 mA/cm^2) and slight increased η_{10} (14.6 mV) after 24 h stability. The DFT calculations further proved optimized intermediate absorbates (*H, *O, *OH and *OOH) adsorption on the NiP-CoP{011} and their rapid desorption for enhanced green H_2 and O_2 production. This work paves the way for the exploration of atomically doped binary metal phosphide on N-containing carbon materials for water electrolysis and other electrocatalysis.

CRediT authorship contribution statement

Adewale K. Ipadeola: Writing – original draft, Methodology, Investigation, Formal analysis, Data curation, Conceptualization. **Mostafa H. Sliem:** Validation, Methodology, Investigation. **Patrick Mwonga:** Validation, Software, Methodology, Investigation. **Kenneth I. Ozoemena:** Writing – review & editing, Validation, Supervision, Methodology. **Aboubakr M. Abdullah:** Writing – review & editing, Validation, Supervision, Resources, Project administration, Funding acquisition.

Declaration of competing interest

The authors declare that they have no known competing financial interests or personal relationships that could have appeared to influence the work reported in this paper.

Acknowledgements

This work was financially supported by the (i) the Qatar National Research Fund (QNRF, a Division of the QRDI Council) through the Academic Research Grant (ARG) program (Grant# ARG01–0524–230330), (ii) Qatar University through an International Research Collaboration Co-Fund program (Grant# IRCC-2023–157) and (iii) National Foundation of Research (NRF), the Department of Science and Innovation (DSI), and the University of the Witwatersrand (Wits) through the DSI-NRF-Wits SARChI Chair in Materials Electrochemistry and Energy Technologies (MEET) (UID No.: 132739). All opinions in the work are those of the authors. The authors thank to the Central Laboratory Units (CLU), Qatar University for SEM, TEM, EDS and SAED, Gas Processing Center (GPC) for XPS analysis, Qatar-Shell Research and Technology Center (QSRTC) for elemental mapping, and the CHPC (Cape Town, South Africa) for granting us unrestricted access to the computing facilities for DFT calculations.

Supplementary materials

Supplementary material associated with this article can be found, in the online version, at doi:10.1016/j.electacta.2024.145236.

Data availability

Data will be made available on request.

References

[1] A.K. Ipadeola, A.B. Haruna, A.M. Abdullah, R.S. Al-Hajri, R. Viter, K.I. Ozoemena, K. Eid, Ternary PdNiO nanocrystals-ornamented porous CeO 2/onion-like carbon for electrooxidation of carbon monoxide: unveiling the effect of supports and electrolytes, Catal. Sci. Technol. 13 (2023) 3035–3046.
[2] A.K. Ipadeola, K. Eid, A.M. Abdullah, Porous transition metal-based nanostructures as efficient cathodes for aluminium-air batteries, Curr. Opin. Electrochem. 37 (2023) 101198.
[3] M.A. Airo, F. Otieno, L. Mxakaza, A. Ipadeola, R.S. Kadzutu-Sithole, L.F. E. Machogo-Phao, C. Billing, M. Moloto, N. Moloto, Probing the stoichiometry dependent catalytic activity of nickel selenide counter electrodes in the redox reaction of iodide/triiodide electrolyte in dye sensitized solar cells, RSC Adv 10 (2020) 39509–39520.
[4] S.H. Park, J. Koo, Y.-J. Park, S. Jang, H.J. Ryu, H. Han, K.T. Lee, Uniformly scalable and stackable porous transport layer manufactured by tape casting and calendering for efficient water electrolysis, Chem. Eng. J. 481 (2024) 148276.
[5] Z. Jiang, G. Yi, X. Yao, Y. Ma, X. Su, Q. Liu, Q. Zhang, Durable and highly-efficient anion exchange membrane water electrolysis using poly (biphenyl alkylene) membrane, Chem. Eng. J. 467 (2023) 143442.
[6] N. Elsayed, M.M. El-Rabiei, M. Negem, F.E.-T. Heakal, The potential of tantalum as an efficient electrocatalyst for green hydrogen production, Electrochim. Acta 404 (2022) 139783.
[7] S.K. Dash, S. Chakraborty, D. Elangovan, A brief review of hydrogen production methods and their challenges, Energies 16 (2023) 1141.
[8] O. Massarweh, M. Al-khuzaei, M. Al-Shafi, Y. Bicer, A.S. Abushaikha, Blue hydrogen production from natural gas reservoirs: a review of application and feasibility, J. CO2 Util. 70 (2023) 102438.
[9] M. Asif, S.S. Bibi, S. Ahmed, M. Irshad, M.S. Hussain, H. Zeb, M.K. Khan, J. Kim, Recent advances in green hydrogen production, storage and commercial-scale use via catalytic ammonia cracking, Chem. Eng. J. 473 (2023) 145381.
[10] H. Zhao, Z.Y. Yuan, Progress and Perspectives for Solar-Driven Water Electrolysis to Produce Green Hydrogen, Adv. Energy Mater. 13 (2023) 2300254.
[11] A.K. Ipadeola, M. Chitt, A. Abdelgawad, K. Eid, A.M. Abdullah, Graphene-based catalysts for carbon monoxide oxidation: experimental and theoretical insights, Int. J. Hydrog. Energy 48 (2023) 17434–17467.
[12] Y. Ma, Z. Zhao, C. Zhang, Y. Zhang, C. Zhang, J. Li, M. Xu, H. Ma, Synergistic reaction kinetics of Pt single atoms/MoS2 and nanoparticles for energy-saving hydrogen production assisted by green electrosynthesis of azotetrazolate compound, Chem. Eng. J. 475 (2023) 146303.
[13] R. Akhter, S. Hussain, S.S. Maktedar, Advanced graphene-based (photo & electro) catalysts for sustainable & clean energy technologies, New J. Chem. 48 (2024) 437–505.
[14] M. Al Murisi, M. Tawalbeh, R. Al-Saadi, Z. Yasin, O. Temsah, A. Al-Othman, M. Rezakazemi, A.G. Olabi, New insights on applications of quantum dots in fuel cell and electrochemical systems, Int. J. Hydrog. Energy 52 (2023) 694–732.
[15] A.K. Ipadeola, A. Abdelgawad, B. Salah, A. Ghanem, M. Chitt, A.M. Abdullah, K. Eid, Self-standing foam-like Pd-based alloys nanostructures for efficient electrocatalytic ethanol oxidation, Int. J. Hydrog. Energy 48 (2023) 30354–30364.
[16] M. Sun, H. Liu, J. Qu, J. Li, Earth-rich transition metal phosphide for energy conversion and storage, Adv. Energy Mater. 6 (2016) 1600087.
[17] A.K. Ipadeola, P.V. Mwonga, S.C. Ray, R.R. Maphanga, K.I. Ozoemena, Bifunctional Behavior of Pd/Ni Nanocatalysts on MOF-Derived Carbons for Alkaline Water-splitting, Electroanalysis 32 (2020) 3060–3074.
[18] A.K. Ipadeola, K.I. Ozoemena, Alkaline water-splitting reactions over Pd/Co-MOF-derived carbon obtained via microwave-assisted synthesis, RSC Adv 10 (2020) 17359–17368.
[19] H. Lei, Q. Wan, S. Tan, Z. Wang, W. Mai, Pt-Quantum-Dot-Modified Sulfur-Doped NiFe Layered Double Hydroxide for High-Current-Density Alkaline Water Splitting at Industrial Temperature, Adv. Mater. 35 (2023) 2208209.
[20] K. Zeng, M. Tian, X. Chen, J. Zhang, M.H. Rummeli, P. Strasser, J. Sun, R. Yang, Strong electronic coupling between single Ru atoms and cobalt-vanadium layered double hydroxide harness efficient water splitting, Chem. Eng. J. 452 (2023) 139151.
[21] S.E. Jun, Y.-H. Kim, J. Kim, W.S. Cheon, S. Choi, J. Yang, H. Park, H. Lee, S.H. Park, K.C. Kwon, Atomically dispersed iridium catalysts on silicon photoanode for efficient photoelectrochemical water splitting, Nat. Commun. 14 (2023) 609.
[22] X. Wang, K. Maeda, A. Thomas, K. Takanabe, G. Xin, J.M. Carlsson, K. Domen, M. Antonietti, A metal-free polymeric photocatalyst for hydrogen production from water under visible light, Nat. Mater. 8 (2009) 76–80.
[23] M. Ashraf, N. Ullah, F. Raziq, I. Khan, K.R. Alhooshani, S.A. Ganiyu, M.N. Tahir, Carbon nitride (C3N3) decorated with non-noble metal Ni2P Co-catalyst based nanocomposites for photocatalytic water splitting, Electrochim. Acta 470 (2023) 143296.
[24] W. Niu, Y. Yang, Graphitic carbon nitride for electrochemical energy conversion and storage, ACS Energy Lett 3 (2018) 2796–2815.
[25] N. Mansor, T.S. Miller, I. Dedigama, A.B. Jorge, J. Jia, V. Brázdová, C. Mattevi, C. Gibbs, D. Hodgson, P.R. Shearing, C.A. Howard, F. Corà, M. Shaffer, D.J.L. Brett, P.F. McMillan, Graphitic Carbon Nitride as a Catalyst Support in Fuel Cells and Electrolyzers, Electrochim. Acta 222 (2016) 44–57.
[26] A. Jaiswal, S. Pal, A. Kumar, R. Prakash, Metal free triad from red phosphorous, reduced graphene oxide and graphitic carbon nitride (red P-rGO-g-C3N4) as robust electro-catalysts for hydrogen evolution reaction, Electrochim. Acta 338 (2020) 135851.
[27] J.L. Fiorio, M.A.S. Garcia, M.L. Gothe, D. Galvan, P.C. Troise, C.A. Conte-Junior, P. Vidinha, P.H.C. Camargo, L.M. Rossi, Recent advances in the use of nitrogen-doped carbon materials for the design of noble metal catalysts, Coord. Chem. Rev. 481 (2023) 215053.
[28] Y. Liu, Q. Wang, J. Zhang, J. Ding, Y. Cheng, T. Wang, J. Li, F. Hu, H.B. Yang, B. Liu, Recent Advances in Carbon-Supported Noble-Metal Electrocatalysts for Hydrogen Evolution Reaction: syntheses, Structures, and Properties, Adv. Energy Mater. 12 (2022) 2200928.
[29] J. Guo, J. Huo, Y. Liu, W. Wu, Y. Wang, M. Wu, H. Liu, G. Wang, Nitrogen-Doped Porous Carbon Supported Nonprecious Metal Single-Atom Electrocatalysts: from Synthesis to Application, Small Methods 3 (2019) 1900159.
[30] W.-Z. Chen, M. Zhang, L. Zhang, J. He, Z. Liu, Y.-Q. Wang, N-doped carbon-coupled nickel nitride species/Ni2P heterostructure for enhancing electrochemical overall water splitting performance, Electrochim. Acta 441 (2023) 141868.
[31] A. Abdelgawad, B. Salah, Q. Lu, A.M. Abdullah, M. Chitt, A. Ghanem, R.S. Al-Hajri, K. Eid, Template-free synthesis of M/g-C3N4 (M = Cu, Mn, and Fe) porous one-

dimensional nanostructures for green hydrogen production, J Electroanal. Chem. 938 (2023) 117426.
[32] J. Li, B. Zhang, Q. Song, X. Xu, W. Hou, Sulfur and molybdenum Co-doped graphitic carbon nitride as a superior water dissociation electrocatalyst for alkaline hydrogen evolution reaction, Ceram. Int. 46 (2020) 14178–14187.
[33] L.-M. Cao, J. Zhang, L.-W. Ding, Z.-Y. Du, C.-T. He, Metal-organic frameworks derived transition metal phosphides for electrocatalytic water splitting, J. Energy Chem. 68 (2022) 494–520.
[34] Y. Gong, J. Yao, P. Wang, Z. Li, H. Zhou, C. Xu, Perspective of hydrogen energy and recent progress in electrocatalytic water splitting, Chin. J. Chem. Eng. 43 (2022) 282–296.
[35] D. Liu, H. Ai, M. Chen, P. Zhou, B. Li, D. Liu, X. Du, K.H. Lo, K.W. Ng, S.P. Wang, Multi-phase heterostructure of CoNiP/CoxP for enhanced hydrogen evolution under alkaline and seawater conditions by promoting H2O dissociation, Small 17 (2021) 2007557.
[36] Q. Zhang, W. Xiao, W.H. Guo, Y.X. Yang, J.L. Lei, H.Q. Luo, N.B. Li, Macroporous array induced multiscale modulation at the surface/interface of Co (OH) 2/NiMo self-supporting electrode for effective overall water splitting, Adv. Funct. Mater. 31 (2021) 2102117.
[37] B. Wang, G. Zhao, Q. Yan, N. Wang, B. Duolihong, H. Xie, X. Xia, Homogeneous pseudoamorphous metal phosphide clusters for ultra stable hydrogen generation by water electrolysis at industrial current density, Chem. Eng. J. 462 (2023) 142138.
[38] Z. Cheng, Y. Xu, B. Fei, Noble metal-free ternary cobalt–nickel phosphides for enhanced photocatalytic dye-sensitized hydrogen evolution and catalytic mechanism investigation, RSC Adv 13 (2023) 23638–23647.
[39] J. Hao, W. Yang, Z. Zhang, J. Tang, Metal–organic frameworks derived Co x Fe 1−x P nanocubes for electrochemical hydrogen evolution, Nanoscale 7 (2015) 11055–11062.
[40] H. Liu, P. He, S. Wang, J. Gao, L. Zhou, C. Li, Y. Zhang, D. Yang, M. He, L. Jia, F. Dong, H. Liu, Facile one-step fabrication of bimetallic Co–Ni–P hollow nanospheres anchored on reduced graphene oxide as highly efficient electrocatalyst for hydrogen evolution reaction, Int. J. Hydrog. Energy 44 (2019) 24140–24150.
[41] Y. Yang, J. Yang, C. Kong, Q. Zhou, D. Qian, Y. Xiong, Z. Hu, Heterogeneous cobalt-iron phosphide nanosheets formed by in situ phosphating of hydroxide for efficient overall water splitting, J. Alloys Compd. 926 (2022) 166930.
[42] L. Zhu, Y. Huang, B. Wang, Y. Zhang, R. Zou, L. Yan, W. Sun, N-doped porous carbon-supported Co x P y/Ni x P y catalyst with enhanced catalytic activity for hydrogen evolution reaction in alkaline solution and neutral seawater, J. Solid State Electrochem. 26 (2022) 233–243.
[43] M. Tong, L. Wang, P. Yu, X. Liu, H. Fu, 3D Network nanostructured NiCoP nanosheets supported on N-doped carbon coated Ni foam as a highly active bifunctional electrocatalyst for hydrogen and oxygen evolution reactions, *Front*, Chem. Sci. Eng. 12 (2018) 417–424.
[44] J.J. Ogada, T.J. Ehirim, A.K. Ipadeola, A.B. Haruna, P.V. Mwonga, A.M. Abdullah, X.-Y. Yang, K. Eid, D.M. Wamwangi, K.I. Ozoemena, Interfacial Electronic Interactions within the Pd-CeO2/Carbon Onions Define the Efficient Electrocatalytic Ethanol Oxidation Reaction in Alkaline Electrolytes, ACS Omega 9 (2024) 7439–7451.
[45] A.K. Ipadeola, P.V. Mwonga, K.I. Ozoemena, Hydrogen oxidation and oxygen reduction reactions on palladium nano-electrocatalyst supported on nickel-deficient MOF-derived carbons, Electrochim. Acta 390 (2021) 138860.
[46] A.K. Ipadeola, P.V. Mwonga, S.C. Ray, R.R. Maphanga, K.I. Ozoemena, Palladium/stannic oxide interfacial chemistry promotes hydrogen oxidation reactions in alkaline medium, ChemElectroChem 7 (2020) 4562–4571.
[47] R. Beltrán-Suito, P.W. Menezes, M. Driess, Amorphous outperforms crystalline nanomaterials: surface modifications of molecularly derived CoP electro (pre) catalysts for efficient water-splitting, J. Mater. Chem. A 7 (2019) 15749–15756.
[48] A.K. Ipadeola, A. Gamal, A.M. Abdullah, A.B. Haruna, K.I. Ozoemena, K. Eid, Pd nanocrystals encapsulated in MOF-derived Ni/N-doped hollow carbon nanosheets for efficient thermal CO oxidation: unveiling the effect of porosity, Catal. Sci. Technol. 13 (2023) 4873–4882.
[49] A.K. Ipadeola, A. Gamal, B. Salah, Y. Ibrahim, A.M. Abdullah, A.B. Haruna, K. I. Ozoemena, K. Eid, Metal-organic Framework-derived Hierarchical Porous N/Co-doped Carbon Supported Sponge-like Pd-SnO2 Nanostructures for Low-temperature CO Oxidation, Mater. Adv. 5 (2023) 2120–2127.
[50] X. Zou, R. Silva, A. Goswami, T. Asefa, Cu-doped carbon nitride: bio-inspired synthesis of H2-evolving electrocatalysts using graphitic carbon nitride (g-C3N4) as a host material, Appl. Surf. Sci. 357 (2015) 221–228.
[51] X. Zhou, Y. Zhu, Q. Gao, S. Zhang, C. Ge, S. Yang, X. Zhong, Y. Fang, Modified graphitic carbon nitride nanosheets for efficient photocatalytic hydrogen evolution, ChemSusChem 12 (2019) 4996–5006.
[52] Z. Yu, Y. Li, J. Qu, R. Zheng, J.M. Cairney, J. Zhang, M. Zhu, A. Khan, W. Li, Enhanced photoelectrochemical water-splitting performance with a hierarchical heterostructure: co3O4 nanodots anchored TiO2@P-C3N4 core-shell nanorod arrays, Chem. Eng. J. 404 (2021) 126458.
[53] J. Gao, Y. Gao, K. Li, H. Tang, Y. Wang, Z. Wu, Searching for highly efficient multifunctional electrocatalysts based on the single metal doped graphitic carbon nitride, Mol. Phys. 119 (2021) e1973606.
[54] Y. Gong, L.-H. Xu, J. Li, D. Shan, Confinement of transition metal phosphides in N, P-doped electrospun carbon fibers for enhanced electrocatalytic hydrogen evolution, J. Alloys Compd. 875 (2021) 159934.
[55] H. Liu, P. He, S. Wang, J. Gao, L. Zhou, C. Li, Y. Zhang, D. Yang, M. He, L. Jia, Facile one-step fabrication of bimetallic Co–Ni–P hollow nanospheres anchored on reduced graphene oxide as highly efficient electrocatalyst for hydrogen evolution reaction, Int. J. Hydrog. Energy 44 (2019) 24140–24150.
[56] A.K. Ipadeola, M.-S. Balogun, A.M. Abdullah, The advancement of porous bimetal nanostructures for electrochemical CO2 utilization to valuable products: experimental and theoretical insights, Carbon Capture Sci. Technol. 13 (2024) 100266.
[57] M. Streckova, O. Petrus, A. Guboova, R. Orinakova, V. Girman, C. Bera, M. Batkova, M. Balaz, J. Shepa, J. Dusza, Nanoarchitectonics of binary transition metal phosphides embedded in carbon fibers as a bifunctional electrocatalysts for electrolytic water splitting, J Alloys Compd 923 (2022) 166472.
[58] Z. Liu, T. Zhang, Y. Lin, H. Jia, Y. Wang, Y. Wang, G. Zhang, Highly N-Doped Fe/Co Phosphide Superstructures for Efficient Water Splitting, Small (2023) 2302475.
[59] X. Ding, W. Uddin, H. Sheng, P. Li, Y. Du, M. Zhu, Porous transition metal phosphides derived from Fe-based Prussian blue analogue for oxygen evolution reaction, J. Alloys Compd. 814 (2020) 152332.
[60] J. Wang, F. Ciucci, In-situ synthesis of bimetallic phosphide with carbon tubes as an active electrocatalyst for oxygen evolution reaction, Appl. Catal. B 254 (2019) 292–299.
[61] X. Zhou, Y. Zi, L. Xu, T. Li, J. Yang, J. Tang, Core–shell-structured Prussian blue analogues ternary metal phosphides as efficient bifunctional electrocatalysts for OER and HER, Inorg. Chem. 60 (2021) 11661–11671.
[62] D.D. Babu, Y. Huang, G. Anandhababu, M.A. Ghausi, Y. Wang, Mixed-metal–organic framework self-template synthesis of porous hybrid oxyphosphides for efficient oxygen evolution reaction, ACS Appl. Mater. Interfaces 9 (2017) 38621–38628.
[63] N.L.W. Septiani, Y.V. Kaneti, K.B. Fathoni, K. Kani, A.E. Allah, B. Yuliarto, H.K. Dipojono Nugraha, Z.A. Alothman, D. Golberg, Self-assembly of two-dimensional bimetallic nickel–cobalt phosphate nanoplates into one-dimensional porous chainlike architecture for efficient oxygen evolution reaction, Chem. Mater. 32 (2020) 7005–7018.
[64] D. Cao, H. Xu, D. Cheng, Construction of defect-rich RhCu nanotubes with highly active Rh3Cu1 alloy phase for overall water splitting in all pH values, Adv. Energy Mater. 10 (2020) 1903038.
[65] G. Ma, P. Guo, S. Wang, Y. Liu, Y. Xin, H. Li, R. Chen, A. Wang, One-step plasma nitriding synthesis of NixN/NF (x= 3, 4) for efficient hydrogen evolution, Appl. Surf. Sci. 561 (2021) 149972.
[66] J. Lee, A. Kumar, T. Yang, X. Liu, A.R. Jadhav, G.H. Park, Y. Hwang, J. Yu, C. T. Nguyen, Y. Liu, Stabilizing the OOH* intermediate via pre-adsorbed surface oxygen of a single Ru atom-bimetallic alloy for ultralow overpotential oxygen generation, Energy Environ. Sci. 13 (2020) 5152–5164.
[67] R. He, L. Yang, Y. Zhang, X. Wang, S. Lee, T. Zhang, L. Li, Z. Liang, J. Chen, J. Li, A CrMnFeCoNi high entropy alloy boosting oxygen evolution/reduction reactions and zinc-air battery performance, Energy Stor. Mater. 58 (2023) 287–298.